Optics Letters

Silicon bowtie structure based adjustable nonrigid all-nonmetal metamaterial terahertz filter

Danni Hao,[1] Yi Zhang,[1] Dongxun Yang,[1] Rui Li,[1] Dan Zhao,[2] Zhenzhen Zhang,[1] Shuai Wang,[1] Wei Jin,[1] Hao Tian,[1] Jiaying Duan,[1] Fei Fan,[2] Shengjiang Chang,[2,3] Ramiro Maro,[1] and Lei Ma[1,*]

[1] Tianjin International Center for Nanoparticles and Nanosystems, Tianjin University, Tianjin 30072, China
[2] Institute of Modern Optics, Nankai University, Tianjin Key Laboratory of Micro-scale Optical Information Science and Technology, Tianjin 300350, China
[3] e-mail: sjchang@nankai.edu.cn
*Corresponding author: lei.ma@tju.edu.cn

Received 28 September 2022; revised 26 October 2022; accepted 31 October 2022; posted 1 November 2022; published 17 November 2022

An all-nonmetal metamaterial (ANM) terahertz device with a silicon bowtie structure has been developed, which has comparable efficiency to that of its metallic counterparts, and better compatibility with modern semiconductor fabrication processes. Moreover, a highly tunable ANM with the same structure was successfully fabricated through integration with a flexible substrate, which demonstrated large tunability over a wide frequency range. Such a device can be used in terahertz systems for numerous applications, and is a promising substitute for conventional metal-based structures.

https://doi.org/10.1364/OL.471704

Introduction. Terahertz (THz) radiation is electromagnetic radiation spanning the frequency range from 0.1 to 10 THz. This frequency regime has attracted particular interest, owing to its nonionizing photon energy, large penetration depth, and broad available bandwidth [1,2]. These make it suitable for a variety of applications, such as material analysis, medical diagnostics, biochemical sensing, imaging, and wireless communications [3–8]. In the last three decades, there has been significant progress in the technology of manipulating THz radiation, driven by the introduction of THz metamaterials, whose electromagnetic responses can be tailored [9,10]. They are artificially structured materials made from sub-wavelength scale elements (meta-atoms) with manmade lattice periodicities and symmetries, which can realize a variety of unconventional properties, therefore providing some unexpected solutions to problems caused by a lack of natural materials with the required functions in the THz band [11,12].

Conventional metallic metamaterials exploit such metals as gold, silver, and copper [13,14], which are expensive and could lead to a vast amount of waste and damage to the environment without proper treatment. Conversely, metamaterials made of nonmetal materials have the advantage of the low cost of primary materials, such as silicon, which has very high compatibility with conventional semiconductor fabrication procedures [15]. Developing metamaterials with nonmetal materials, i.e., all-nonmetal metamaterials (ANMs), have not been fully explored in the field yet, except for the so-called all-dielectric metamaterials [16]. All-dielectric metamaterials are usually made of high-index dielectric materials, such as undoped silicon. They manipulate electromagnetic waves through low-order dipole or multiple Mie resonances. Conversely, highly doped silicon can support surface plasmon polaritons (SPPs), just like metallic materials. It has been used to replace metal in some metamaterial designs to achieve a broadband response [17]. Among various nonmetal materials, silicon, possessing the advantages of high index, low cost, and mature fabrication techniques, has attracted much attention. Fan *et al.* [18] proposed silicon-based ANM THz absorbers and used them for uncooled THz imaging. By tailoring the geometry of the cylindrical silicon structures, the resonance frequencies of magnetic and electric dipole modes inside resonators are merged and achieve impedance matching to free space. Taking advantage of doped silicon's surface plasmons, single-layer broadband absorbers have been designed [17]. The performance of an absorber can be tuned through optical excitation and its sensing ability has also been demonstrated. Silicon-based ANMs have also been used for beam shaping, i.e., wavefront engineering, using the fact that a phase shift can be imparted when the resonator is excited by an incident wave. A full 2π phase control was realized by Ma *et al.* [19] for resonators made from silicon cubes on a silica substrate with carefully designed geometry. It demonstrated that the single-layer metamaterial can generate vortex and Bessel beams in reflection and undoubtedly has vast potential applications in the next generation of THz wireless communication systems [20].

In this article, we introduce a silicon-based metamaterial filter that is composed of simple bowtie shape structures. A strong field confinement can normally be found in the substrate adjacent to the resonator, to reduce insertion and dissipation losses; therefore, polydimethylsiloxane (PDMS) is adopted as the substrate, owing to its low permittivity and low losses across a broad THz range. Moreover, its elasticity makes such a device mechanically flexible.

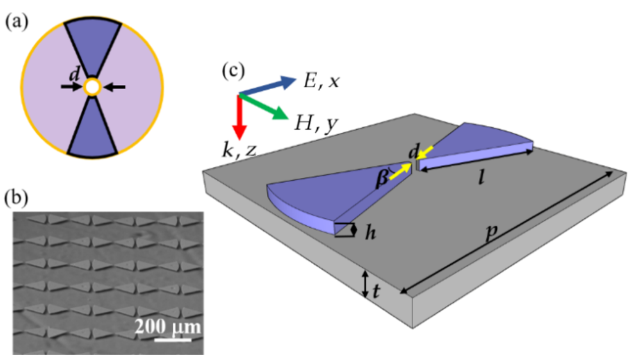

Fig. 1. All-nonmetal bowtie shape with geometric parameters: $h = 10\,\mu\text{m}$. Inset: top view of bowtie-shaped silicon antennas, which are sectors of a ring. Yellow lines indicate the inner and outer circles of the ring.

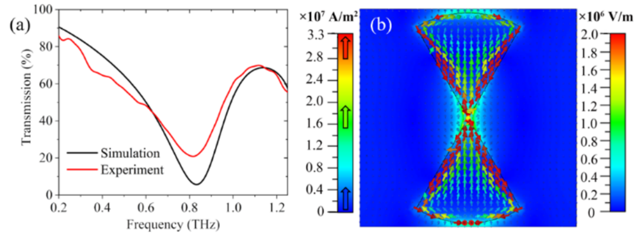

Fig. 2. (a) Simulated and measured transmission spectra of metamaterial. (b) Simulated top view of (colored arrows) current densities and (background color) electric field distribution (with color bar on right) at a frequency of 0.834 THz.

Since it is hard to grow silicon directly on polymer amorphous substrates, a transfer procedure has been developed to fabricate the silicon-PDMS hetero-material device. To explore its THz response, the structural parameter dependent properties have been investigated systematically. Both numerical simulation and experimental results indicate that the device effectively functions as a filter in the THz range and that the resonance frequency can be fully tuned by changing the geometry of the lattice structure. Resembling conventional metallic metamaterials, the proposed highly doped silicon-based filter can be scaled to other frequency ranges.

Design and methods. The designed all nonmetallic metamaterial is shown, schematically, in Fig. 1. It is composed of a periodic lattice of symmetric silicon sectors on a PDMS substrate. The two symmetric sectors are sectors of a ring with internal diameter d and outer radius $d/2 + l$. The periodic lengths along the x and y axes are indicated by p. The thickness of the PDMS substrate layer is $30\,\mu\text{m}$. The incident THz wave transmitted through the dielectric metamaterial structure is linearly polarized along the x axis.

Boron-doped silicon was chosen for the resonator, since it exhibits a relatively high permittivity across the THz frequency range, whose value is described by the Drude model as $\varepsilon = \varepsilon_c - \omega_p^2/(\omega^2 + i\gamma\omega)$, where ε_c=11.68 is the relative permittivity at infinite frequency. The plasma frequency $\omega_p = 49.4236$ THz, and the collision frequency $\gamma = 11.1784$ THz [21]. To investigate the performance of the metamaterial, numerical simulations were conducted using the commercial software CST Microwave Studio. Its finite-element frequency domain solver was used and the unit cell boundary condition was applied to the x and y axes to model an infinite two-dimensional array. Transmission was obtained from the calculated S-parameters, where $T(\omega) = |S_{21}|^2$. The permittivity of PDMS was set to 1.72, with a loss tangent of 0.15 around 600 GHz [18,22].

The all-nonmetal meta-atoms were fabricated using a silicon-on-insulator (SOI) wafer with a 10-μm thick device layer and a 1-μm thick buried oxide (BOX) layer (SiO_2). The structure was first patterned using a standard photolithography process, then a 300-nm Al layer was deposited using e-beam evaporation. Following lift-off, the device layer was etched by reactive ion etching (RIE), using Al as the hard mask. To make the release easier, the BOX layer buried underneath the 10-μm silicon layer was then etched by 49% hydrofluoric acid until less than 15-μm wide SiO_2 was left (as shown in Supplement 1, Fig. S1). A 30-μm thick PDMS film was spin-coated on a silicon substrate and an ≈2 mm thick PDMS frame with an 8-mm diameter hole was prepared. After applying an oxygen plasma for activating both the silicon surface and the PDMS film surface, the patterned array was flip bonded on the PDMS film and transferred to the supporting PDMS frame. A schematic illustration of the fabrication process can be found in Supplement 1, Fig. S2. An oblique scanning electron micrograph of the fabricated silicon array and a side view of the etched (pre-bond) sample are shown in Fig. 1(b) and Supplement 1, Fig. S2, respectively. The reactive ion etched sidewall has a positively sloped profile. The final device consists of 28×28 bowtie structures (Supplement 1, Fig. S3).

To investigate the filtering performance of the antenna, the initial parameters were set as $\beta = 60°$, $l = 115\,\mu\text{m}$, and $d = 10\,\mu\text{m}$. The lattice constants along the x and y axes were both set to $p = 250\,\mu\text{m}$. The transmission of the sample was characterized using a THz time-domain spectroscopy (TDS) system, as shown in Supplement 1, Fig. S4. The incident wave passed a linear polarizer first and was then focused under normal incidence on the device surface through an aperture of ≈3.5 mm in diameter. The measured transmission spectra were normalized by a reference spectrum from a sample of 30-μm thick PDMS film.

The measured transmission spectrum, accompanied by a simulation, is shown in Fig. 2(a). Good agreement is achieved, where the mismatch is mainly due to the scattering from the periodic metamaterial and fabrication offsets, including geometric dimensions, sloped sidewall, and surface roughness [23,24]. To unveil the resonating mechanism of the ANM structure, Fig. 2(b) shows the top view of the current densities and electric field distribution at a resonance frequency of ≈0.83 THz. From Fig. 2(b), it is not difficult to notice that most of the current density is along the straight edges of the sectors and that the current density is greater closer to the gap than near the two arcs; this response is similar to that of metallic resonators. In the latter case, the current is even stronger inside the resonator [21]. The electric field is localized in the small central gap and in the gaps between adjacent bowtie structures through the bottom and top two arcs. The permittivities of gold and doped silicon with varying carrier concentration are characterized using the Drude model. Transmission spectra with different materials were also simulated, as can be seen in Supplement 1, Fig. S5. By increasing the concentration of doping ions, the resonance linewidth narrows and the strength increases, indicating that the highly doped silicon-based structure can give a comparable performance to its metallic counterpart made of gold.

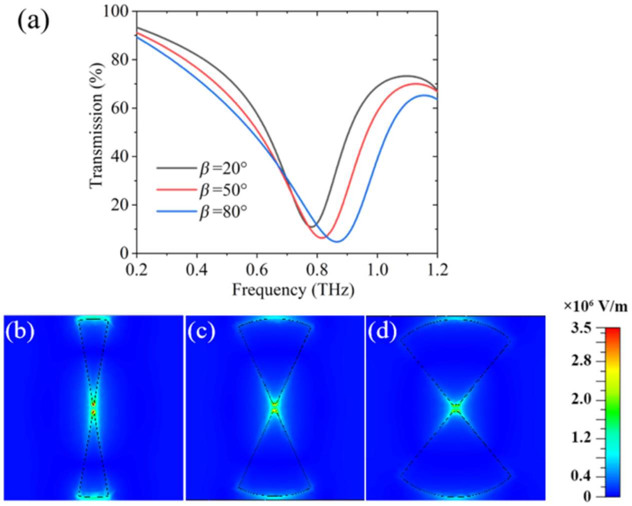

Fig. 3. (a) Simulated transmission spectra of ANM structure arrays with $\beta = 20°$, $50°$, and $80°$. The incident wave is polarized along the axis of the bowtie resonators. (b) Simulated electric field distribution for three unit cells with different designs at their individual resonant frequencies. The color bar is arranged so that all plots share the same scale.

Discussion. To investigate the structural parameters dependency of the ANM, we start by exploring its performance correlation with the angle β. Figure 3(a) shows that the simulated results of β vary from 20° to 80°. We find that the resonant frequency blueshifts as the angle increases. This can be attributed to the decrease of the effective index of the local SPP [25]. In a simplified model, the short range SPP can be treated as a confined wave traveling inside the resonators and the transverse field distribution profile of the SPP is an analog of the eigenmode of the waveguide with the local cross section vertical to the antenna axis [26]. Using this model, the resonance wavelength of the SPP is determined by the geometry of the antenna length, L, and the effective index of the short range SPP, n_{eff}. For a fundamental half-wave resonance, the resonance wavelength can be described as $\lambda_0 \approx 2\int_{-L/2}^{L/2} n_{\mathrm{eff}}(x)dx + \delta$, where δ is an offset introduced by the gap and the reflection from the two ends. In our case, the antennas have the same length, $L = 2l + d$, and the same gap, d. Therefore, as β increases, the local cross section of the waveguide increases, and the effective index of the local SPP decreases. The effect of structural parameter changes on electric field is shown in Figs. 3(b) to 3(d). This indicates that the electric field intensity decreases with the increase in β. This can be attributed to the two local SPPs, which are confined at two straight sides of the sectors. When they move farther from each other, the coupling effect will be weakened.

The lattice constant of the array, i.e., the period of the unit cells, is anticipated to have a great impact on the collective interactions and the consequent electromagnetic activities [23]. This effect could be exploited for designing tunable devices; as the substrate material PDMS is flexible, the resonance of the ANM structure can be adjusted by changing distances between meta-atoms. To demonstrate the efficient tunability and modulation of the ANM device to the THz wave, the structure's lattice constants are varied by simply stretching the flexible PDMS substrate. As shown in Fig. 4, calculated and measured transmission spectra coincide well, exhibiting a linearly

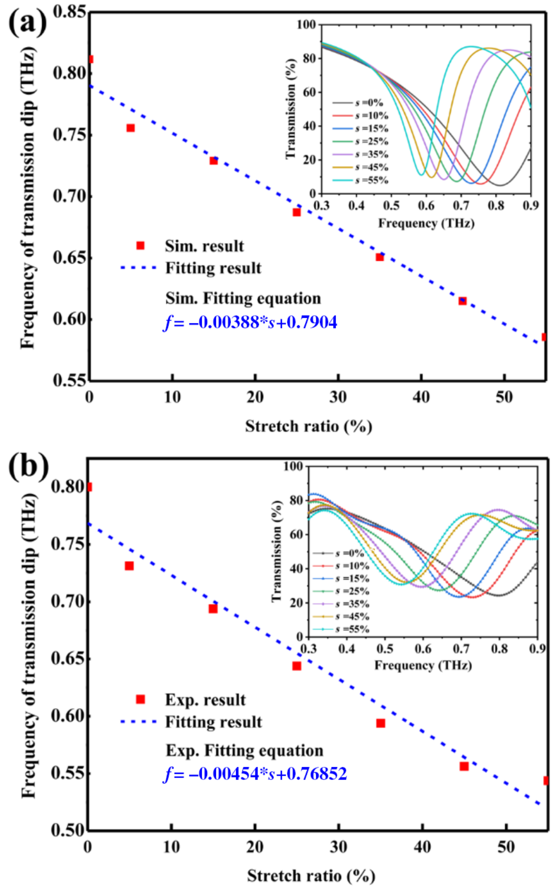

Fig. 4. Stretch ratio dependent transmission spectra, where s ranges from 0% to 55%: (a) simulated; (b) measured. Data can be found in Supplement 1, Table S1.

continuous redshift of the transmission dip from 0.825 THz to 0.585 THz with applied stretch ratio up to 55% along the y direction.

In the stretching process, the transverse strain along the x and z axes can be ignored, owing to the small Poisson's ratio of PDMS [27]. The change in the lattice constant along the y axis, p_y, plays the most important role in the modulating process, while the variation of d only plays a negligible role on the transmission spectra tuning, as demonstrated in Supplement 1, Figs. S6 and S7. Since the geometry of each resonator is unchanging during this process, the shift of the transmission dips can rationally be attributed to the variation of lattice collective interactions. Optical micrographs of the device in resting and stretched states are shown in Supplement 1, Fig. S8. The PDMS membrane allows a stretch ratio up to at least 55% and rapidly restores after release. The intensity variations of the dip can be ascribed to the weakening of collective interactions inside the resonator array, causing the smearing of spectral resonance features.

Conclusion. In summary, a silicon bowtie microstructure based THz filter was designed and fabricated. The structural parameter dependent resonant properties of the filter have been systematically investigated. The results show that the frequency response of ANM filter is highly sensitive to the lattice structure. Accordingly, a flexible PDMS substrate based ANM was manufactured and demonstrates a continuous high and continuous resonance response tunability both of the strength and frequency by simple substrate stretching, which could meet requirements of different practical applications. The results shed light on the resonant mechanisms of dielectric metamaterials and the design of THz radiation modulating devices and sensors [28,29].

Funding. China Postdoctoral Science Foundation (2020M670646); National Key Research and Development Program of China (2020YFC 2004602); National Natural Science Foundation of China (11774255).

Acknowledgments. This work was supported by the National Natural Science Foundation of China under Grant Nos. 11774255 and 11904258, the National Key R&D Program of China No. 2020YFC2004602, and the China Postdoctoral Science Foundation 2020M670646.

Disclosures. The authors declare no conflicts of interest.

Data availability. Data underlying the results presented in this paper are not publicly available at this time but may be obtained from the authors upon reasonable request.

Supplemental document. See Supplement 1 for supporting content.

REFERENCES

1. M. Tonouchi, Nat. Photonics **1**, 97 (2007).
2. Z. Chen, X. Ma, B. Zhang, Y. Zhang, Z. Niu, N. Kuang, W. Chen, L. Li, and S. Li, China Commun. **16**, 1 (2019).
3. M. Zhang, D. Hao, S. Wang, R. Li, S. Wang, Y. Ma, R. Moro, and L. Ma, Opt. Express **30**, 14651 (2022).
4. C. J. Strachan, P. F. Taday, D. A. Newnham, K. C. Gordon, J. A. Zeitler, M. Pepper, and T. Rades, J. Pharm. Sci. **94**, 837 (2005).
5. E. P. J. Parrott, Y. Sun, and E. Pickwell-MacPherson, J. Mol. Struct. **1006**, 66 (2011).
6. H. Guerboukha, K. Nallappan, and M. Skorobogatiy, Adv. Opt. Photonics **10**, 843 (2018).
7. I. F. Akyildiz, J. M. Jornet, and C. Han, Phys. Commun. **12**, 16 (2014).
8. J. Federici and L. Moeller, J. Appl. Phys. **107**, 111101 (2010).
9. H.-T. Chen, J. F. O'Hara, A. J. Taylor, R. D. Averitt, C. Highstrete, M. Lee, and W. J. Padilla, Opt. Express **15**, 1084 (2007).
10. M. Kenney, J. Grant, Y. D. Shah, I. Escorcia-Carranza, M. Humphreys, and D. R. S. Cumming, ACS Photonics **4**, 2604 (2017).
11. H. Němec, P. Kužel, F. Kadlec, C. Kadlec, R. Yahiaoui, and P. Mounaix, Phys. Rev. B **79**, 241108 (2009).
12. W. Xu, L. Xie, and Y. Ying, Nanoscale **9**, 13864 (2017).
13. J. Li, C. M. Shah, W. Withayachumnankul, B. S.-Y. Ung, A. Mitchell, S. Sriram, M. Bhaskaran, S. Chang, and D. Abbott, Appl. Phys. Lett. **102**, 121101 (2013).
14. N. R. Han, Z. C. Chen, C. S. Lim, B. Ng, and M. H. Hong, Opt. Express **19**, 6990 (2011).
15. C. Li, P. Yu, Y. Huang, Q. Zhou, J. Wu, Z. Li, X. Tong, Q. Wen, H.-C. C. Kuo, and Z. M. Wang, Prog. Surf. Sci. **95**, 100584 (2020).
16. S. Jahani and Z. Jacob, Nat. Nanotechnol. **11**, 23 (2016).
17. Y. Wang, D. Zhu, Z. Cui, L. Hou, L. Lin, F. Qu, X. Liu, and P. Nie, ACS Omega **4**, 18645 (2019).
18. K. Fan, J. Y. Suen, X. Liu, and W. J. Padilla, Optica **4**, 601 (2017).
19. Z. Ma, S. M. Hanham, P. Albella, B. Ng, H. T. Lu, Y. Gong, S. A. Maier, and M. Hong, ACS Photonics **3**, 1010 (2016).
20. D. Headland, T. Niu, E. Carrasco, D. Abbott, S. Sriram, M. Bhaskaran, C. Fumeaux, and W. Withayachumnankul, IEEE J. Sel. Top. Quantum Electron. **23**, 8500918 (2017).
21. Y. Z. Cheng, W. Withayachumnankul, A. Upadhyay, D. Headland, Y. Nie, R. Z. Gong, M. Bhaskaran, S. Sriram, and D. Abbott, Adv. Opt. Mater. **3**, 376 (2015).
22. A. Podzorov and G. Gallot, Appl. Opt. **47**, 3254 (2008).
23. F. Xie, W. Wu, M. Ren, W. Cai, and J. Xu, Adv. Opt. Mater. **8**, 1901435 (2020).
24. Y. Yang, I. I. Kravchenko, D. P. Briggs, and J. Valentine, Nat. Commun. **5**, 5753 (2014).
25. W. Ding, R. Bachelot, S. Kostcheev, P. Royer, and R. Espiau de Lamaestre, J. Appl. Phys. **108**, 124314 (2010).
26. W. Ding, R. Bachelot, R. Espiau de Lamaestre, D. Macias, A.-L. Baudrion, and P. Royer, Opt. Express **17**, 21228 (2009).
27. S. Dogru, B. Aksoy, H. Bayraktar, and B. E. Alaca, Polym. Test. **69**, 375 (2018).
28. S. Zhang, X. Zhu, H. Shi, Y. Wang, Z. Chen, and H. Duan, Appl. Opt. **58**, 6295 (2019).
29. K. Liu, R. Zhang, Y. Liu, X. Chen, K. Li, and E. Pickwell-Macpherson, Biomed. Opt. Express **12**, 1559 (2021).